Numerical Simulations for the F-16XL Aircraft Configuration

Alaa Elmiligui[1] and Khaled Abdol-Hamid[2]
NASA Langley Research Center, Hampton, VA, 23681, USA

Peter A. Cavallo[3]
Combustion Research and Flow Technology, Pipersville, PA 18947, USA

Edward B. Parlette[4]
ViGYAN, Inc., Hampton, Virginia 23666

Numerical simulations of flow around the F-16XL are presented as a contribution to the Cranked Arrow Wing Aerodynamic Project International II (CAWAPI-II). The NASA Tetrahedral Unstructured Software System (TetrUSS) is used to perform numerical simulations. This CFD suite, developed and maintained by NASA Langley Research Center, includes an unstructured grid generation program called VGRID, a postprocessor named POSTGRID, and the flow solver USM3D. The CRISP CFD package is utilized to provide error estimates and grid adaption for verification of USM3D results. A subsonic high angle-of-attack case flight condition (FC) 25 is computed and analyzed. Three turbulence models are used in the calculations: the one-equation Spalart–Allmaras (SA), the two-equation shear stress transport (SST) and the kε turbulence models. Computational results, and surface static pressure profiles are presented and compared with flight data. Solution verification is performed using formal grid refinement studies, the solution of Error Transport Equations, and adaptive mesh refinement. The current study shows that the USM3D solver coupled with CRISP CFD can be used in an engineering environment in predicting vortex-flow physics on a complex configuration at flight Reynolds numbers.

I. Nomenclature

Cp	surface pressure coefficient	α	angle of attack
M_∞	free stream Mach number	δj	first cell height, in
Rn	Reynolds number based on reference chord		
U	free stream reference velocity, ft/sec		

Acronyms

CAWAP	Cranked Arrow Wing Aerodynamics Program	NATO	North Atlantic Treaty Organization
CAWAPI	Cranked Arrow Wing Aerodynamics Program, International	RTO	Research and Technology Organization
ETE	Error Transport Equation		

[1] Research Engineer, Configuration Aerodynamics Branch, Mail Stop 499, AIAA Senior Member.
[2] Research Engineer, Configuration Aerodynamics Branch, Mail Stop 499, AIAA Associate Fellow.
[3] Senior Research Scientist, AIAA Associate Fellow.
[4] Research Engineer, 30 Research Drive.

II. Introduction/Background

The Cranked Arrow Wing Aerodynamic Project International (CAWAPI) utilized the F-16XL aircraft as part of a basic research project planned in support of the High Speed Research Program (HSRP). A review of the project and how it evolved over the years is given by Lamar & Obara [1]. Flight, wind tunnel and computational studies were conducted, and various data sets were generated, analyzed, and compared to CFD results [2-5]. CAWAPI objectives were to validate new methodologies, to evaluate a number of predictive methods against available flight test data at high Reynolds numbers, and to check the technology readiness level (TRL) of Computational Fluid Dynamics (CFD) codes for a military aircraft. Military requirements result in a need for a better understanding of the aircraft characteristics before full-scale production. For this purpose, new and existing CFD codes have to be validated, and their TRL checked and/or increased. CAWAPI members embraced the idea of engaging in a cooperative venture. The benefits from validated CFD codes can enhance the analysis of system performance prior to flight, as well as tools to aid in the understanding of unexpected flight behavior. CFD results showed good comparison with flight data except for flight condition (FC) 25 and FC 70 [3-5]. FC 25 is a subsonic high angle-of-attack case at flow conditions of $M_\infty = 0.242$, $\alpha = 19.84°$, and $Rn = 32.22 \times 10^6$ based on reference chord length. FC 70 is a transonic low angle-of-attack case where $M_\infty = 0.97$, $\alpha = 4.37°$, $Re = 88.77 \times 10^6$. For FC 25, the worst agreement between computed results and flight data was on the outboard wing panel where there were strong interactions between the vortices shed from the inboard wing panel, actuator pod, air dam, and crank. The reason for discrepancy was attributed to possible flow unsteadiness and turbulence model failure to capture vortex breakdown on the inboard wing panel. The CAWAPI-1 recommendation was to generate better grids, with improved density to capture vortical flow, to adapt to flow features and to use higher fidelity physical models.

The present paper is part of the CAWAPI-2. This is an international cooperation with contributions from several organizations. The objective is to find out why CFD fails to simulate these two flight condition cases. Relevant questions include:

1) What is the best flow physics based model or “turbulence model” to employ?
2) Do we need to adapt for vortical flow generated at these conditions?
3) Do we have a grid converged simulation?
4) What is the correct geometry for the transonic case FC 70?

Due to limited time and resources, the present study focused on the subsonic high angle-of-attack case, FC 25. The current study addresses the first three questions noted above, while the fourth concern will be fully addressed in future work. Other groups [6-12] within CAWAPI-2 will examine these issues as well as whether there is any aero-elasticity issue that affects the fourth question. In the present paper, the NASA Tetrahedral Unstructured Software System [13] (TetrUSS) flow solver, named USM3D, is used to present detailed comparisons of surface pressures for FC 25 condition. The results produced by the one-equation Spalart–Allmaras (SA), the two-equation SST, and the kε turbulence models are compared with flight data. An error estimation package developed with funding from a NASA Small Business Innovation Research (SBIR) project is used to analyze the CFD results and provides guidance to the limit of turbulence models used. Grid adaption and uncertainty quantification using the commercial code CRISP CFD was conducted and is also presented.

III. Computational Approach

In this section, details of the computational grids and the numerical approach used in this study are presented. Various convergence criteria adopted to ensure solution convergence are described.

USM3D Flow Solver

USM3D is a tetrahedral cell-centered, finite volume, Euler and Navier-Stokes flow solver. Time

integration follows the implicit point Gauss-Seidel algorithm, explicit Runge-Kutta approach, and local time stepping for convergence acceleration. The solver scheme allows various options for computing the inviscid flux quantities across each cell face. These include Roe's flux-difference splitting (FDS), advection upstream splitting method (AUSM), flux vector splitting (FVS), and the Harten, Lax, and van Leer with contact restoration (HLLC) scheme. MinMod and Superbee flux limiters have been incorporated in the flow solver to smooth out the flow discontinuities due to shock waves. Turbulence models include Spalart-Allmaras (SA) [14] with and without the wall function, shear stress transport (SST) [15] and kε.[16].

Grid Generation

The surface triangulations along with the field tetrahedral volume grids were generated using the GRIDTOOL and VGRID software developed at NASA Langley Research Center (LaRC). A rectangular box that encompasses the vehicle is typically used to define the computational domain far-field boundaries. Each face of this rectangular box is located several body lengths away from the configuration in the upstream, radial and downstream direction. The farfield boundaries were located at 100 times the mean aerodynamic chord of the wing. As a general practice, each final converged solution is analyzed to insure that the laminar sub-layer, has been grid resolved and that the average y^+ is less than 1. Four different grids (extra coarse, coarse, medium, and fine) have been generated to facilitate grid-converged solutions. Table 1 provides the average normal spacing to viscous wall in terms of y^+ coordinate, the values of the first cell height δ_j, the total number of cells in the viscous layer, and the total number of surface elements for different grids.

Table 1: Grids and computational resources.

Grid	Number of cells	First cell height, δ_1, in	Y+ average	Number of viscous cells	Number of surface triangles	Number of iterations	Number of CPU
Coarse	19,370,847	0.0009225	1.108	15,193,683	256,846	50,000	288
Medium	62,473,588	0.000615	0.757	40,200,735	640,850	50,000	720
Fine	143,034,292	0.00041	0.516	83,173,422	1,265,352	50,000	1200

Error Quantification

Typical grid refinement studies, while effective in quantifying the discretization error inherent in any CFD solution, are often intensive in terms of time, labor, and CPU cost. As a supplement to such studies, solution verification is performed using an Error Transport Equation (ETE) solver contained in the CRISP CFD package. The ETE method [17-19] has been developed for use with various unstructured grid solvers, including USM3D. The basic premise of the ETE is that discretization errors may be generated in one location of the domain and convected elsewhere as erroneous waves propagated by the characteristics of the Euler/Navier-Stokes equations, where they become apparent and manifest as interpolation errors. The source term of the ETE is formed from the leading terms of the truncation error associated with the inviscid flux scheme. Once the ETE solution is obtained, errors in any number of local or integrated quantities may be examined [18].

The inclusion of numerical error bars as part of post-processing and analysis offers new possibilities for how CFD results can be interpreted and used. If the increments provided by grid refinement can be reliably predicted, a higher level of confidence may be placed in lower fidelity meshes. This would potentially preclude the need for fine grid analysis if the numerical errors predicted for a medium resolution mesh were judged to be acceptable. In addition, if grid-induced errors are bounded and experimental data lies outside numerical error bars, it would likely indicate a deficiency in physical modeling. Such information would be of considerable benefit to the CFD analyst in evaluating simulation results.

Adaptive Mesh Refinement and Coarsening

CRISP CFD contains a parallel mesh adaptation and quality improvement capability for three-dimensional mixed-element unstructured meshes [20-21]. Meshes comprised of tetrahedral, prismatic, and hexahedral regions may be readily modified to generate more accurate flow solutions through local refinement and coarsening. Tetrahedral refinement and coarsening are accomplished using Delaunay refinement and edge collapse methods, while cell subdivisions are employed for viscous tetrahedra, pyramids, prisms, and hexahedral cells. Upon completing the mesh modifications, the solution is interpolated onto the adapted mesh using a grid-transparent procedure based on nearby point clouds [22].

An estimate of the solution error is used to drive mesh adaptation. For steady state applications, the default method currently employed [21] is an interpolation error, based on forming a higher order approximation of the solution at each mesh point using a least squares approach. The difference between the higher order reconstruction from incident nodes and the current solution forms the error indicator. If the current mesh is sufficiently fine to support the spatial variation in the solution, the estimated error will be low, allowing coarsening to take place. Conversely, a high degree of error indicates that additional refinement is needed. This approach has proven successful in a variety of applications and is capable of detecting shear layers, separation, vortical flows, and weak gradients in coarse regions, as well as shocks and expansions, with no tuning required of the user . If an Error Transport Equation solution is available, it is also possible to use the residual of the ETE to drive mesh refinement [18].

Solution Development and Convergence

All solutions are computed using Roe's flux difference splitting method. Flow is assumed to be fully turbulent. Three turbulence models, the SA, the SST and kε, will be used in the present computations. Mean flow and turbulence model equations were solved in a decoupled fashion. In the precursor studies, not reported herein, it was established that the solutions were insensitive to the manner in which they were advanced in time (steady-state versus 2nd order time-accurate) and to the prescription of an initial state (freestream condition versus converged solution at a lower angle-of-attack). Based on these findings all solutions were obtained assuming steady state using the implicit backward-Euler scheme.

In general, solution convergence is evaluated by monitoring variations in all six longitudinal and lateral force and moment aerodynamic coefficients. A solution was considered converged when fluctuations in these coefficients were reduced to less than 0.5% of their respective average values calculated over the previous 2000 iterations. Additionally, all solutions were required to have the cumulative mean flow residual errors reduced by at least three orders of magnitude and turbulence model residual errors reduced by at least two orders of magnitude. Each case completed 10,000 first-order iterations followed by 40,000 second-order iterations for a total of 50,000 iterations. A sample of convergence history is shown in Fig. 1a. The solution achieved 5-orders of magnitude reduction and all six force and moment coefficients were converged. Switching from a first-order to a second-order scheme caused the spike in the residual at 10,000 iterations. A NAS supercomputer was used to compute all of the cases. A typical case was completed in less than 12 hours.

IV. Results and Discussions

The subsonic high angle-of-attack flight condition (FC 25) is simulated for the flow around the F-16XL. Computational results, surface static pressures, are presented and compared with flight data. FC 25 has a free stream Mach number of 0.242, an angle of attack of 19.4 degrees, and Reynolds number equal to 32.22×10^6 based on reference chord length. Vortical-flow phenomena over the upper surface, is expected. The F-16XL has two leading edge sweep angles, 70° for the inboard wing panel and 50° for the outboard wing panel. It should be noted that all simulations were conducted as steady RANS calculations and this approach might mask unsteadiness effects.

The F16XL surface pressure distribution is shown in Figure 1b. The flow structure consists of several vortices: i) an inboard vortex originating from the wing apex, ii) an outboard primary vortex

originating from the wing leading edge outboard of the crank, and iii) an airdam vortex. All solutions exhibit convergence to 4-orders of magnitude.

Figure 1c shows the surface streamlines. The convergence-divergence of the surface streamlines lines shows the location of the flow separation and reattachment. Flight data were extracted at different fuselage stations (FS) and butt line (BL) cuts. Surface pressure measurements are extracted at various FS and BL locations for comparison with flight test data. The black lines in figure 1d shows the seven FS locations, 185, 300, 337.5, 375, 407.5, 450 and 492.5. Figure 1e shows the seven BL locations: 55, 70, 80, 95, 105, 153.5 and 184.5. BL 184.5 is highlighted in red as it presents a great challenge for turbulence model results to match flight data and will be discussed in this section. The primary vortex starts at FS 185 and the secondary vortex starts at around FS 407.5. There are strong interactions in the vortex system over the F-16XL. The inner-wing secondary vortex strikes the airdam followed by an airdam vortex emanating downstream. Figures 1a and 1b show the outer-wing primary vortex forming at the crank and traveling downstream and outboard towards the tip and the missile store.

In the following sections, we demonstrate the effects of grid refinement and turbulence models in predicting the locations and strengths of these vortices. During the last 10 years of NASA's involvement with CAWAPI, several grids were produced to understand the aerodynamic characteristics of all the flight conditions for the F16XL configuration. Table 1 above lists the coarse, medium and fine grids, that were used in the present study. We utilized these grids for turbulence models comparisons, grid comparisons, grid adaption and error estimates. The 62 million cell "medium" grid was used as a baseline resolution mesh for the assessment of turbulence modeling effects.

Turbulence Model Comparisons

Data were extracted at seven BL locations: 55, 70, 80, 95, 105, 153.5 and 184.5 (figure 1c). Seven FS locations, 185, 300, 337.5, 375, 407.5, 450 and 492.5 (figure 1d) were also available for comparison. The pressure coefficient data from the well-established one-equation SA turbulence model, the SST model and the kε two-equation model were compared, with FC 25 data and presented in Figure 2. In general, all three turbulence models compared well with flight data on the lower surface of the wing however, it is clear that kε provides the best comparisons with upper surface pressure data as shown Figure 2. Figure 2g, is the only BL cut that all three turbulence models fails to predict the first 30% of the chord. This is the outboard BL cut along the wingspan with the smallest chord length, shown as a red line in figure 1d. For the other BL and FS cuts, kε results compared well with the flight data. On the other hand, both SA and SST gave similar results and over-predict the data similar to the results shown in figure 2f.

The surface pressure coefficient from kε and SA turbulence models are shown in figure 3. The kε results are less diffusive than SA results. The streamlines, at BL 105, superimposed on the total pressure contours are shown in figure 4 to envision the discrepancies between the results of SA and kε turbulence models. The pressure results from kε slowly increased in the first 20% length of the wing (see figure 2e) following the flight data. Also, the kε total pressure is much smaller compared with SA results. This causes the streamlines to be pushed down toward the wing surface causing the pressure to slowly increase as compared with the streamlines from SA that completely missed the wing surface.

In the following sections, having performed model validation, solution verification exercises consisting of grid comparisons, error-estimates and attempts to adapt the grid are discussed in detail.

Grid Comparisons

Four different grids (extra coarse, coarse, medium, and fine) have been used to facilitate grid-converged solutions. The extra coarse grid was the original grid used in reference [4]. Three new grids were generated for the F-16XL; coarse, medium and fine. The guidelines established by the Drag Prediction Workshop [23] and the High Lift Prediction Workshop [24], to address solution sensitivity to grid refinement, were adopted in the grid generation. The prior computations for FC 25, reference [4], on the extra coarse grid, provided the reference data for the present analysis and, in particular, for generating the properly sized coarse, medium, and fine grid levels. Figure 5 shows the representative computational grids on the surface and the near-field view for typical cross sectional cuts of the coarse, medium, and

fine grid. Table 1 above provides the values of δ_1, the total number of cells in the viscous layer, and the total number of surface elements for different grids. A factor of 2/3 was used to size the value of δ_1, for each consecutive grid refinement. Furthermore, a factor of 1.26 was used to construct the viscous layers (δ_j) in the radial direction by setting the grid growth rate parameters R1 = 0.16 and R2 = 0.04 for all the grids used in the present investigation.

$$\delta_j = \delta_1 (1+R1(1+R2)^{j-1})^{j-1}$$

In this equation, the variable δ_1 is the first cell height next to the solid surface in the normal direction. This grid system is suitable for cell-centered flow solvers.

In an effort to improve the grid quality, a grid optimization technique [23] available in CRISP CFD was employed to smooth out any local grid skewness or large variation of the cell volumes before the launching of the flow solver. This activity was shown to stabilize and enhance the solution convergence characteristics. In addition, as shown in Table 1, there was roughly the expected linear relationship between the total number cells (N) and the corresponding computer resource requirements. As a result, the medium grid computations required approximately 3.2 times the CPU hours to converge the solution as those needed for the coarse grid. This similarity in computer usage remained approximately the same between the medium and the fine grid.

The original grid from CAWAPI I study had a 10.2 million-cells grid with a y+ average of 1.2. The grid did not follow the criteria of the Drag Prediction Workshop and is not shown in Table 1. More details about this grid can be found in reference [4]. Figure 5 shows the computational grid distribution on the surface of the F16XL and two sample cuts at FS 185 and BL 184.5 for the coarse, medium, and fine grids. There were 15 components, with different sizes and shapes over the F16XL configuration. Such geometrical complexity presented a challenge for the grid generation and the flow solver to properly capture the associated flow physics and the resulting aerodynamic properties of the vehicle.

Figure 6 shows comparison between the computed surface pressures from rom the CAWAPI-1 grid, the coarse, medium, and fine grids, and the measured surface pressures at selected stations BL 70, BL 105, BL 184.5, and FS 300. The surface pressures at BL 70, BL 105, and FS 300 show little effect of grid refinement. At these three stations, coarse, medium and fine grid surface pressures are almost identical and grid convergence was achieved. In general all computed results are in good agreement with the measured data. This is also evident for all the other stations that are not shown in Figure 6. Grid resolution effect can be clearly seen further outboard on the main wing at station BL 184.5. Even fine grid surface pressures show poor agreement with the measured surface pressures at this station and grid convergence was not achieved. The reason for the discrepancy might be due to kε turbulence model failure to predict vortex break down and the onset of separation on the outer wing. Vortex breakdown was expected but since steady RANS calculations were performed it might have masked the development of unsteady separation. To further investigate this discrepancy, higher fidelity approaches (URANS, LES, or DES simulations) must be used.

Error Estimates

An example of using error quantification for the F-16XL configuration is discussed in this section. The results were used to predict the error bar for surface pressure at different stations along the configuration. The solution of the error equations will require computer time equivalent to solving the main equations. Once the error equations are solved, it is possible to generate error data for most aerodynamic quantities of interest. It is expected that these errors would reduce with mesh refinement as the vortex resolution is improved. Furthermore, the errors predicted on a coarse or medium resolution mesh should contain the fine grid solution.

Figure 7 presents predicted errors in pressure coefficient due to grid resolution at selected butt line and fuselage station locations for the coarse 19M-cell grid. The medium resolution 62M cell results are included for comparison. At nearly each station shown, the predicted errors from the solution of the ETE span the observed differences between coarse and medium grid solutions. This provides a quantitative assessment of the increment expected from refining the mesh, and serves to verify the computation and

bound the error due to discretization. Even the vortex reattachment at FS 185, seen in Figure 7e, is nearly accounted for by the predicted errors.

A similar error analysis is depicted in Figure 8 for the 62M-cell medium resolution mesh. Results from the 143M cell fine grid are included for comparison. The observed solution increment is well captured by the predicted error bars for each of the four butt line locations considered in Figure 8a-8d. The fuselage station comparisons indicate areas where the predicted errors fall short of properly containing the fine grid results, as evident in Figure 8e, 8g, and 8h, where the inner and outer primary vortices and the dam vortex are better resolved. One explanation for the discrepancy is that the ETE is solved on the same discretization as the flow solution itself, and thus is subject to similar numerical diffusion issues. Thus it is important to match the limiter, gradient evaluation, flux scheme, etc. between the flow solver and the ETE solver to the greatest extent possible. It should also be noted that while not present in this example, the ETE cannot account for flow features present on one grid and absent in another. That is, the simulations must produce self-similar solutions to place confidence in the solution verification provided by the error analysis.

Figure 9 depicts simultaneous visualization of pressure coefficient and its associated error using the "error bubble" technique [18], in which spherical glyphs are colored by the selected variable and sized according to the magnitude of the error. In the limit, the glyphs vanish in regions of negligible error. This technique allows grid-induced errors to be readily rendered and assessed for complex flows. In Figure 9 it is apparent that much of the error due to grid resolution is associated with the leading edge vortices. Local grid adaptation holds the potential to reduce and minimize such errors and will be explored in the following section.

Adaptive Grid

In the current study, two approaches were used in the grid adaption. The first was the default solution error estimation method implemented in CRISP CFD, which is based on forming a higher order approximation of the solution at each mesh point using a least squares approach [21]. If the current mesh was sufficiently fine to support the spatial variation in the solution, the estimated error was low, allowing coarsening to take place. Conversely, a high degree of error indicated additional refinement was needed. The second approach used information from the ETE solver to drive the mesh adaptation process [18]. This method of adaptation would not necessarily refine the flow features. It should be noted that since the criterion for coarsening was the same as that used for refinement, keying adaptation to a single variable might have removed cells in regions where other variables may have exhibited significant variation. One also must be cautious with any coarsening when using error sources. This is an area that still needs to be explored.

CRISP CFD was used to evaluate the flow field variation, refine, coarsen, and optimize the mesh in a localized manner, and also produced a new, adapted grid and interpolated solution file for the selected flow solver. USM3D was then restarted on the newly adapted grid and ran until fully converged. This constituted one cycle of adaption. Ideally, mesh adaptation allows one to obtain more accurate, grid-converged solutions in an efficient manner. Given a converged solution on an initial mesh, subsequent solutions on locally adapted meshes do not require as much computational expense to re-establish a converged state. In steady state simulations, adaptation may be repeated as often as desired, until grid convergence is achieved or solution errors are below a defined tolerance.

In this study, three adaption cycles were conducted. Table 2 shows grid size after each adaption cycle. Grid sizes increased from 19 million cells on the original coarse grid to 24 million cells for the final adapted mesh. The degree of refinement was not aggressive, and in the interest of retaining practical mesh sizes, the viscous cell layers were not modified. Viscous cell subdivision [20] tends to increase the number of cells dramatically, as cells are split into 2, 4, or 8 cells according to predefined patterns. As a consequence of freezing the viscous layers, the surface mesh was not modified in the present calculations.

Table 2: Grids used in the mesh adaptation studies.

Grid	Number of cells
Original Mesh	19,370,847
1st Adaptation	20,189,477
2nd Adaptation	21,553,095
3rd Adaptation	24,299,853
Adaptation Using ETE Sources	25,420,230

Figure 10 presents comparison between Cp distribution on the different adapted grid levels and the solution on the coarse and medium grids at selected FS and BL locations. Figure 10 shows slight variations between all three adapted grid levels and the 19M cell coarse grid. As the mesh was adaptively refined, it is evident that the solution is moving towards a grid converged result. Figure 10a shows that the adapted solution did not capture Cp at the wing leading edge. However adapted solution captured Cp peak at x/c of 0.19. The adaption outperformed the medium grid in capturing expansion over the wing between x/c of 0.19 and 0.3. The adapted and the medium grid solutions are in close agreement for x/c >0.3 yet higher than flight data for x/c > 0.6. Figure 10b shows adapted solution is closer to flight data than the medium grid solution, yet still failed to capture the Cp distribution on the leading part of the wing. As the mesh was adaptively refined, the peak around 2y/b of 0.8, at station FS 185, moved toward medium grid solution as shown in figure 10c. Figure 10d shows that the adaptive solutions, at FS 300, were grid converged and in close agreement with medium grid results. FS 300 is one of the stations where the computed results are grid converged as shown earlier in Figure 6d comparing coarse, medium and fine results. The differences observed between the medium grid results and the adapted mesh solutions may be attributed to the fact that the surface mesh was not modified in the adaptive grid sequence; hence resolution of the vortex reattachment was not enhanced. It is anticipated that allowing the viscous cell layers to be subdivided would alleviate this issue, and this may be explored in future work.

V. Conclusion

The results for the F-16XL configuration obtained using the TetrUSS flow analysis and CRISP CFD systems are presented. The flow analysis was conducted for a subsonic, high angle-of-attack case, where $M_\infty = 0.242$, $\alpha = 19.84°$, $Re = 32.22 \times 10^6$ based on the reference chord length. The configuration was the focus of the Cranked Arrow Wing Aerodynamic Project International II (CAWAPI-2). All the computed results were based on the assumption that the flow was fully turbulent and steady over the entire vehicle surfaces. Turbulence model sensitivity of the numerical results was examined using the SA, SST and kε turbulence models. Computed surface pressures were compared with corresponding flight data. In general, the kε results compared well with the flight data, while both SA and SST gave similar results that over-predicted the data. It was observed that the accuracy of the computed surface pressure, from SA, SST and kε turbulence models, was degraded closer to the wing tip region. Surface pressures at BL 184.5 span were substantially under-predicted over most of the main wing cut. It is surmised either a higher fidelity turbulence model or detached eddy simulation (DES) may improve the accuracy in resolving the wing tip vortex and localized flow separation on the outer wing. Grid convergence study was conducted for kε turbulence model and it showed that the solution was grid converged.

Solution verification was approached using two methods, prediction of the discretization errors using the solution of Error Transport Equations (ETE), and local adaptive mesh refinement. The ETE solutions were useful in quantifying the error due to grid resolution on coarse and medium level meshes. Including the numerical error bars allow for the discrepancies with the test data to be better understood as due to physical modeling issues vs. resolution issues. Adaptive refinement reduced the resolution error and confirmed that a grid converged result was achieved. Adaptive refinement on the coarse grid captured medium grid results. The areas for future investigation include viscous layers and surface mesh refinement, the use of error prediction and adaptive refinement for the transonic FC 70 case, and gaining additional experience with the ETE source criterion for adapting the grid.

Acknowledgments

The authors would like to thank Susan Cliff and Michael Aftosmis from NASA Ames for the fruitful discussions during the course of this work.

VI. References

[1] Obara, C. J., and Lamar, J. E., "Overview of the Cranked-Arrow Wing Aerodynamics Project International," Journal of Aircraft, Vol. 46, No. 2, 2009, pp. 355–368.
[2] Lamar, J. E., Obara, C. J., Fisher, B. D., and Fisher, D. F., "Flight, Wind-Tunnel, and Computational Fluid Dynamics Comparison for Cranked Arrow Wing (F-16XL-1) at Subsonic and Transonic Speeds," NASA TP 2001-210629, Feb. 2001.
[3] Boelens, O. J., Badcock, K. J., Elmilgui, A., Abdol-Hamid, K. S., and Massey, S. J., "Comparison of Measured and Block Structured Simulations for the F-16XL Aircraft," Journal of Aircraft, Vol. 46, No. 2, 2009, pp. 377–384.
[4] Görtz, S., Jirásek, A., Morton, S. A., McDaniel, D. R., Cummings, R. M., Lamar, J. E., and Abdol-Hamid, K. S., "Standard Unstructured Grid Solutions for CAWAPI F-16XL," Journal of Aircraft, Vol. 46, No. 2, 2009, pp. 385–408.
[5] Rizzi, A., Jirásek, A., Lamar, J. E., Crippa, S., Badcock, K. J., Boelens, O. J., "Lessons Learned from Numerical Simulations of the F-16XL Aircraft at Flight Conditions," Journal of Aircraft, Vol. 46, No. 2, 2009, pp. 423–441.
[6] James M. Luckring; Arthur W. Rizzi, "Toward Improved CFD Predictions of Slender Airframe Aerodynamics Using the F-16XL Aircraft (CAWAPI-2):, to be presented in 52nd AIAA Aerospace Sciences Meeting, National Harbor, Maryland, January 13–17, 2014.
[7] Maximilian M. Tomac; Adam Jirasek; Arthur W. Rizzi, "Factors Influencing Accurate Shock Vortex Interaction Prediction on F-16XL Aircraft", to be presented in 52nd AIAA Aerospace Sciences Meeting, National Harbor, Maryland, January 13–17, 2014.
[8] Adam Jirasek; Luca Cavagna; Luca Riccobene; Sergio Ricci; Arthur W. Rizzi, "Estimating first-order aeroelastic effects on F-16XL using NeoCASS/Edge analysis", to be presented in 52nd AIAA Aerospace Sciences Meeting, National Harbor, Maryland, January 13–17, 2014.
[9] Adam Jirasek; Maximilian M. Tomac; Arthur W. Rizzi, "Improved Predictions for high Angle of Attack Flow around the F-16XL Aircraft", to be presented in 52nd AIAA Aerospace Sciences Meeting, National Harbor, Maryland, January 13–17, 2014.
[10] Okko J. Boelens; James M. Luckring, "Flow Analysis of the F-16XL Aircraft (CAWAPI-2) At Transonic Flow Conditions", to be presented in 52nd AIAA Aerospace Sciences Meeting, National Harbor, Maryland, January 13–17, 2014.
[11] Stephan M. Hitzel, "Vortex Flows of the F-16XL Configuration - CAWAPI-II Free-Flight Simulations", to be presented in 52nd AIAA Aerospace Sciences Meeting, National Harbor, Maryland, January 13–17, 2014.
[12] Arthur W. Rizzi ,"What was Learned in Predicting Slender Airframe Aerodynamics with the F16-XL Aircraft", to be presented in 52nd AIAA Aerospace Sciences Meeting, National Harbor, Maryland, January 13–17, 2014.
[13] TetrUSS Web page: http://tetruss.larc.nasa.gov/usm3d/index.html, May 2013.
[14] Spalart, P. R., Allmaras, S.R.: A One-Equation Turbulence Model for Aerodynamic Flows. AIAA Paper No. 1992-0439.
[15] Menter, F. R., "Improved Two-Equation k-omega Turbulence Models for Aerodynamic Flows", NASA TM103975, October 1992.
[16] Jones, W. P., and Launder, B. E., "The Prediction of Laminarization With a Two-Equation Model of Turbulence," Int. J. Heat & Mass Transf., vol. 15, no. 2, Feb. 1972, pp. 301-314.
[17] Cavallo, P. A., and Sinha, N., "Error Quantification for Computational Aerodynamics Using an Error Transport Equation," Journal of Aircraft, Vol. 44, No. 6, 2007, pp. 1954-1963.
[18] Cavallo, P. A., O'Gara, M. R., and Schikore, D. R., "Software System for Prediction, Visualization, Analysis, and Reduction of Errors In CFD Simulations," AIAA Paper 2009-3649, 19th AIAA Computational Fluid Dynamics Conference, San Antonio, TX, June 22-25, 2009.
[19] Cavallo, P. A., O'Gara, M. R., Feldman, G. M., and Liu, Z., "Unified Error Transport Equation Solver for Solution Verification on Unstructured Grids," AIAA Paper 2012-3345, 42nd Fluid Dynamics Conference, New Orleans, LA, June 25-28, 2012.
[20] Cavallo, P. A., and Grismer, M. J., "A Parallel Adaptation Package for Three-Dimensional Mixed-Element Unstructured Meshes," *Journal of Aerospace Computing, Information, and Communication*, Vol. 2, No. 11, 2005, pp. 433-451.
[21] Cavallo, P. A., Sinha, N., and Feldman, G. M., "Parallel Mesh Adaptation Method for Moving Body Applications," *AIAA Journal*, Vol. 43, No. 9, 2005, pp. 1937-1945.
[22] Baker, T. J., "Interpolation from a Cloud of Points," *Proceedings of the 12th International Meshing Roundtable*, Santa Fe, NM, September 14-17, 2003.
[23] Baker, T. J., and Vassberg, J. C., "Tetrahedral Mesh Generation and Optimization," *Proc. 6th International Conference on Numerical Grid Generation*, ISGG, pp. 337-349, 1998.
[24] 5th AIAA CFD Drag Prediction Workshop, AIAA, New Orleans, LA, http://aaac.larc.nasa.gov/tsab/cfdlarc/aiaa-dpw// [retrieved 21 November 2013].

[25] 2nd AIAA CFD High Lift Prediction Workshop (HiLiftPW-2), AIAA, San Diego, CA, http://hiliftpw.larc.nasa.gov/ [retrieved 21 November 2013].

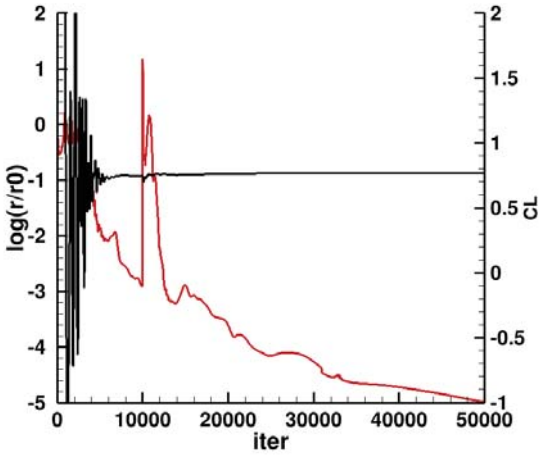

a) Convergence history

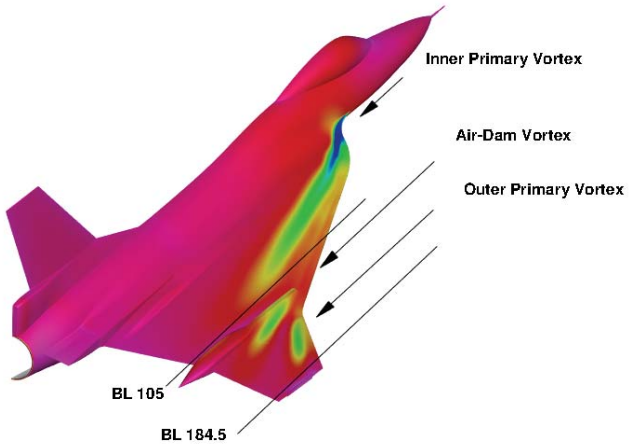

b) Surface pressure distribution

c) Surface streamlines

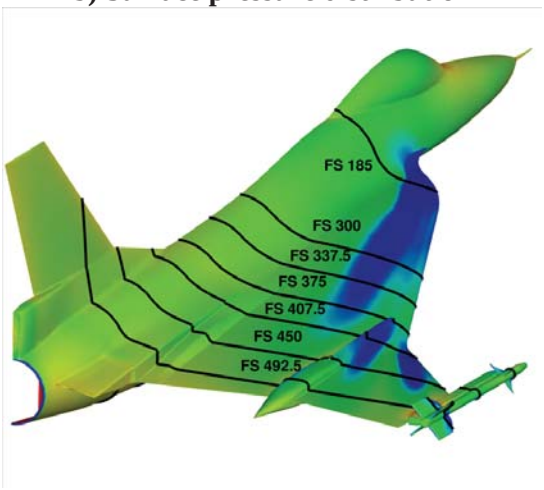

d) Fuselage stations

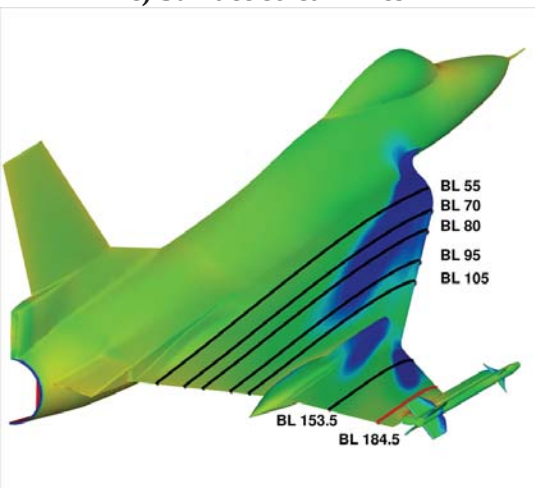

e) Butt lines

Figure 1. USM3D solution of the F16XL at M_∞ = 0.242, α = 19.84°, and Rn = 32.2x10^6.

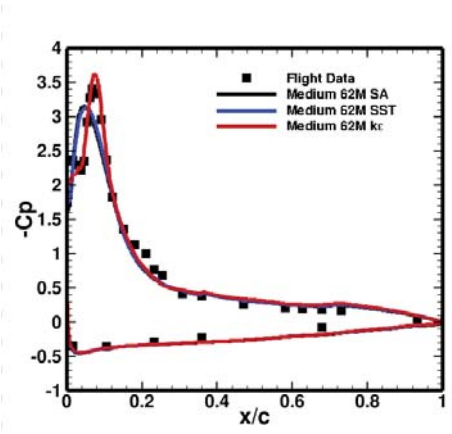

(a) BL 55

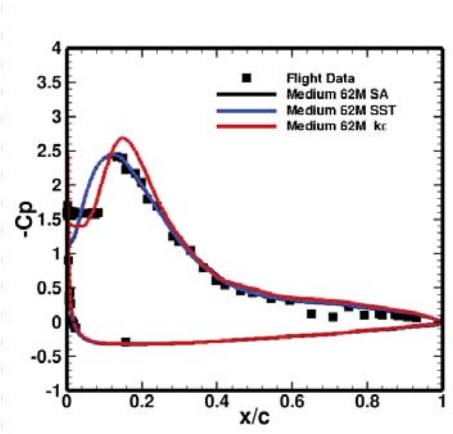

(b) BL 70

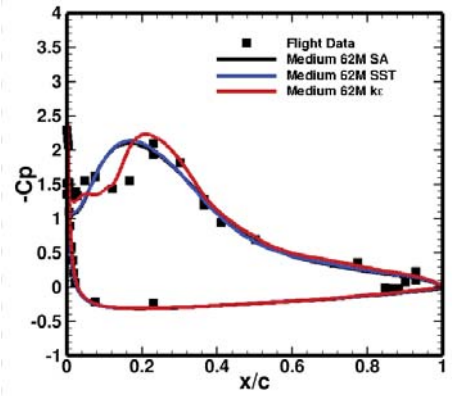

(c) BL 80

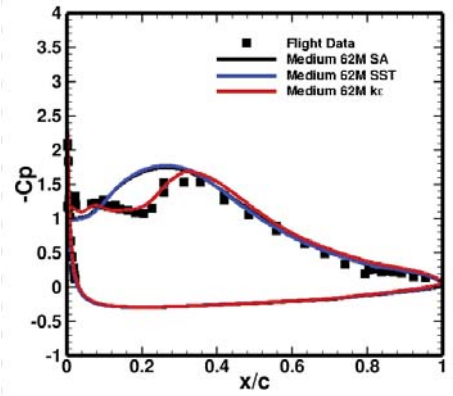

(d) BL 95

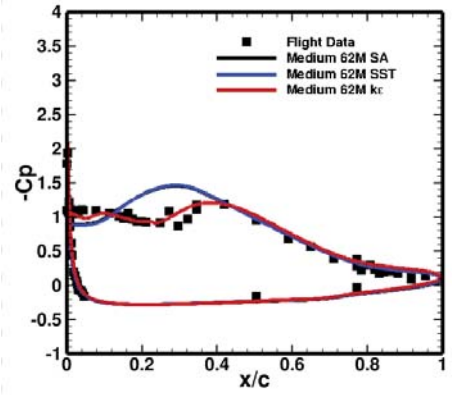

(e) BL 105

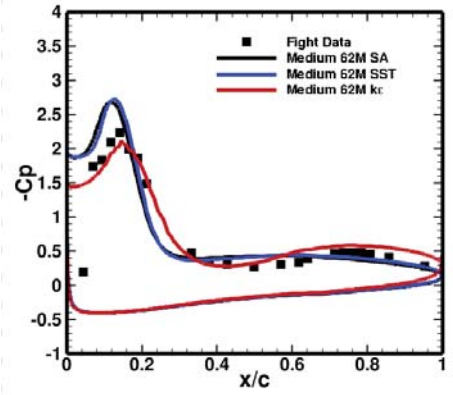

(f) BL 153.5

Figure 2. Comparisons of computed turbulence model results and measured flight C_p at FC 25 (M_∞ = 0.242, α = 19.84°, and Rn= 32.2 x 10^6).

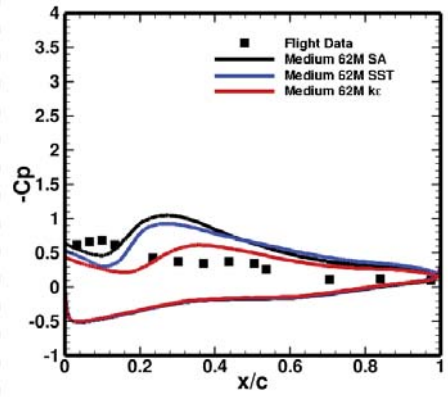

(g) BL 184.5

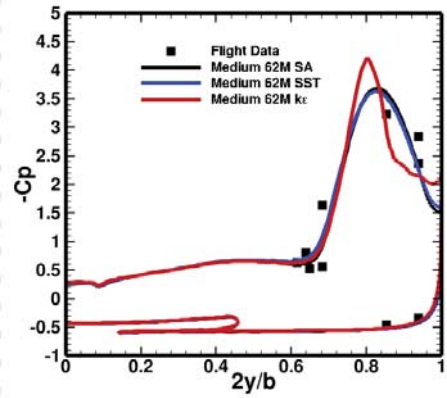

(h) FS 185

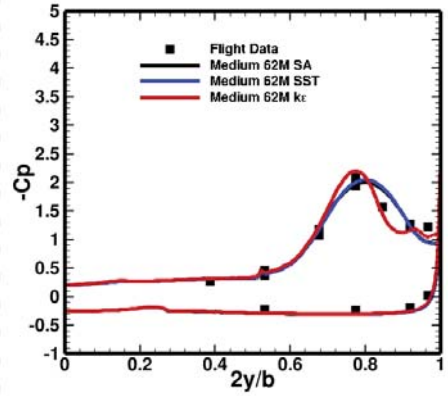

(i) FS 300

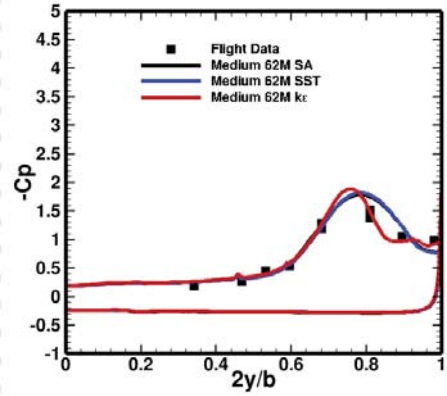

(j) FS 337.5

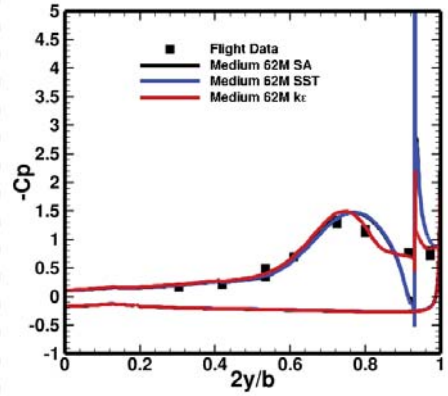

(k) FS 375

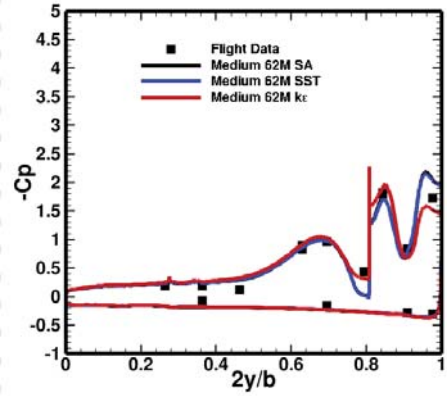

(l) FS 407.5

Figure 2. Continued.

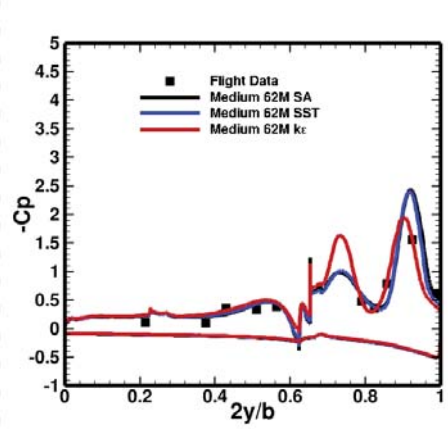

(m) FS 450

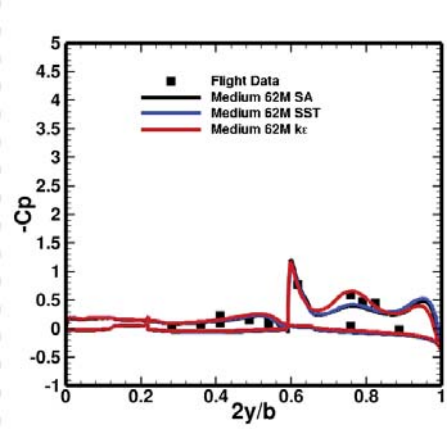

(n) FS 492.5

Figure 2. Concluded.

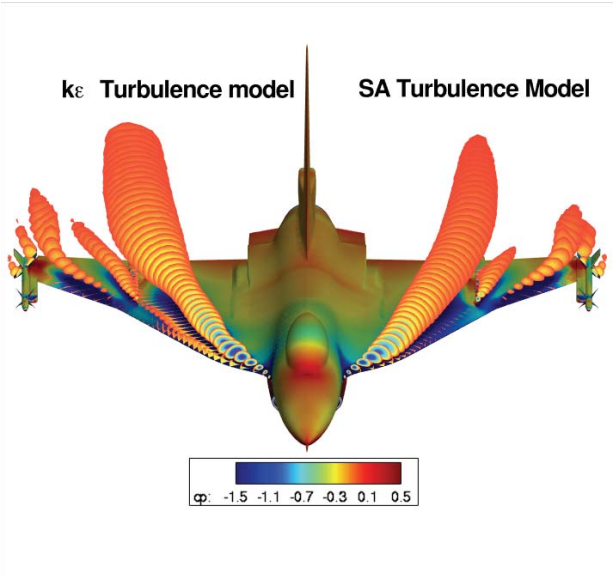

Figure 3. Comparisons of upper surface C_p using SA and kε models at FC 25 (M_∞ = 0.242, α = 19.84°, and Rn= 32.2 x 10^6).

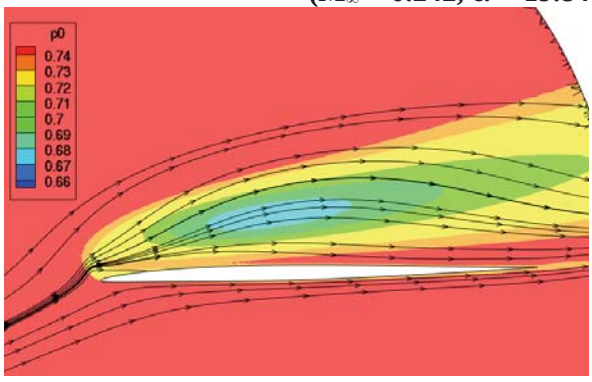

a) BL 105, SA

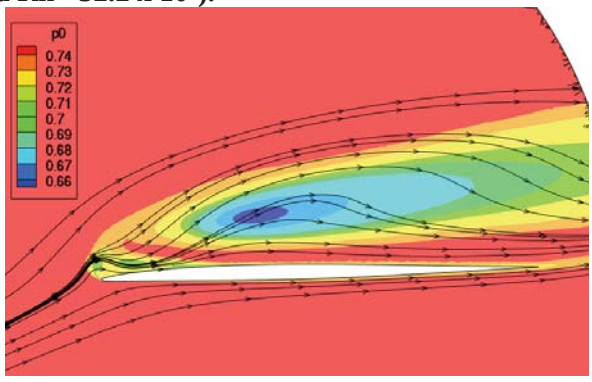

b) BL 105, kε

Figure 4. Computed total pressure and streamlines at BL 105 for FC 25 using SA and kε models (M_∞ = 0.242, α = 19.84°, and Rn= 32.2 X 10^6).

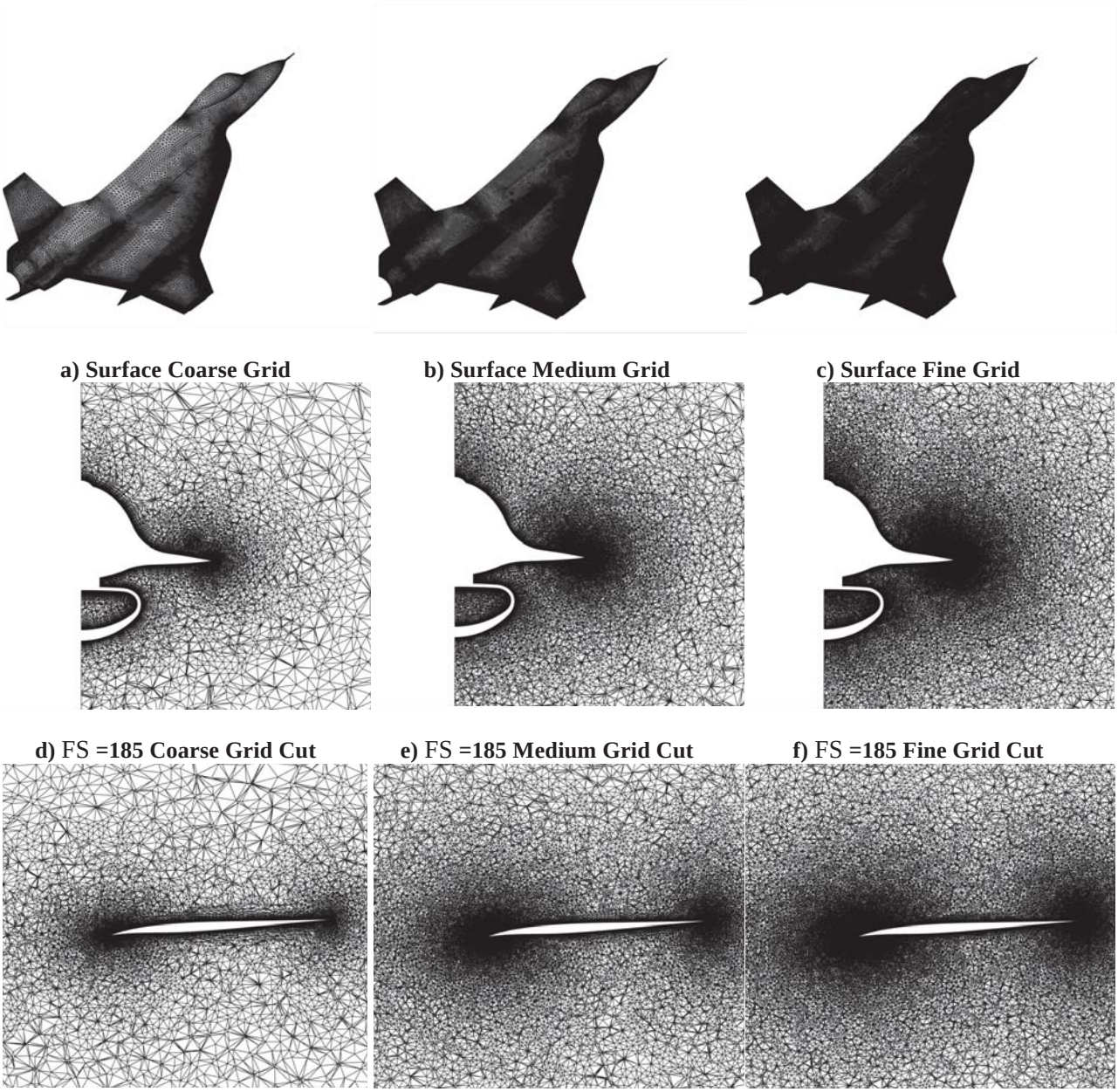

a) Surface Coarse Grid **b) Surface Medium Grid** **c) Surface Fine Grid**

d) FS **=185 Coarse Grid Cut** **e)** FS **=185 Medium Grid Cut** **f)** FS **=185 Fine Grid Cut**

g) BL **=184.5 Coarse Grid Cut** **h)** BL **=184.5 Medium Grid Cut** **i)** BL **=184.5 Fine Grid Cut**

Figure 5. Computational grid distribution on the surface and at FS 185 and BL 184.5 for the coarse, medium, and fine grids.

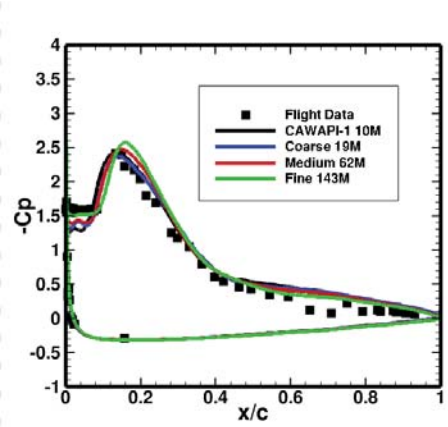

(a) BL 70

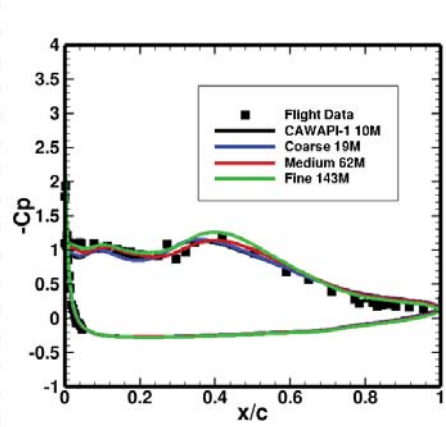

(b) BL 105

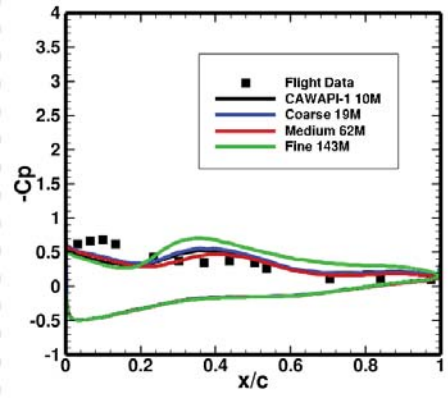

(c) BL 184.5

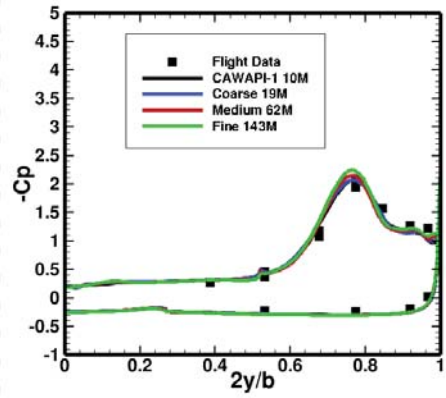

(d) FS 300

Figure 6. Comparisons of flight data with kε turbulence model Cp on different grid levels (M_∞ = 0.242, α = 19.84°, Rn= 32.2 X 10^6).

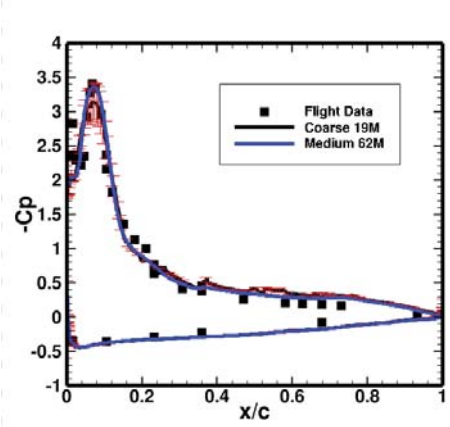

(a) BL 55

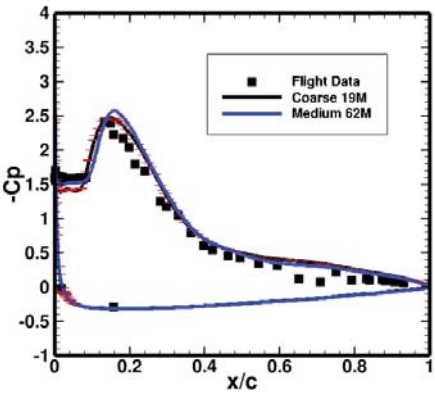

(b) BL 70

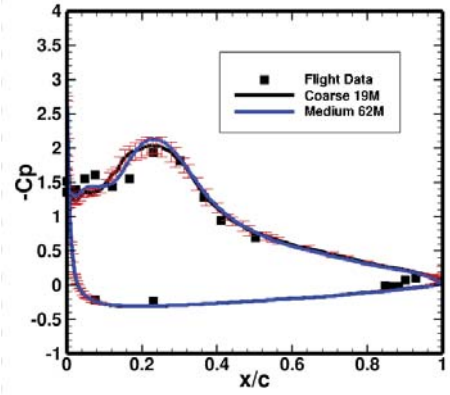

(c) BL 80

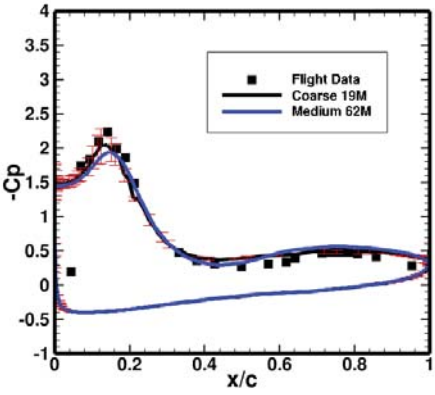

(d) BL 153.5

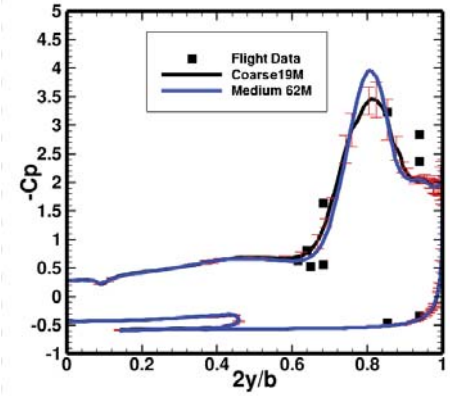

(e) FS 185

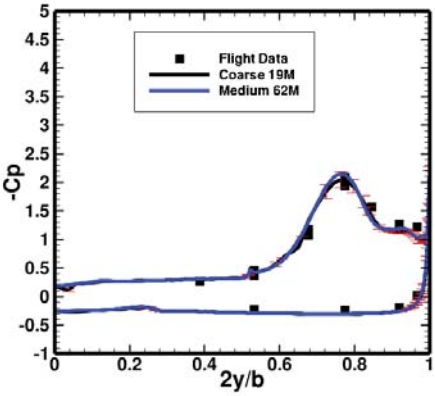

(f) FS 300

Figure 7. Computed error estimates on 19M-cell mesh compared with 62M-cell medium mesh results (M_∞ = 0.242, α = 19.84°, Rn= 32.2 X 10^6, kε turbulence model).

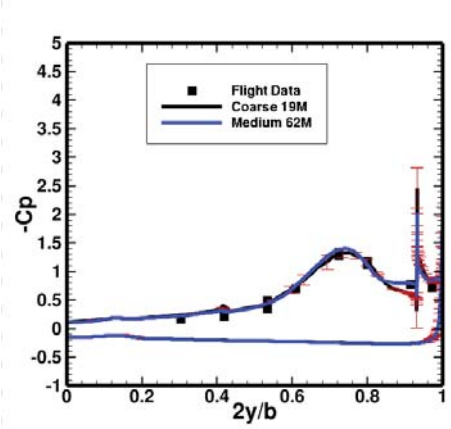

(g) FS 375

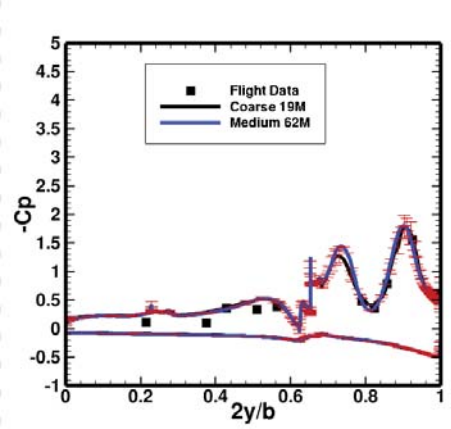

(h) FS 450

Figure 7. concluded.

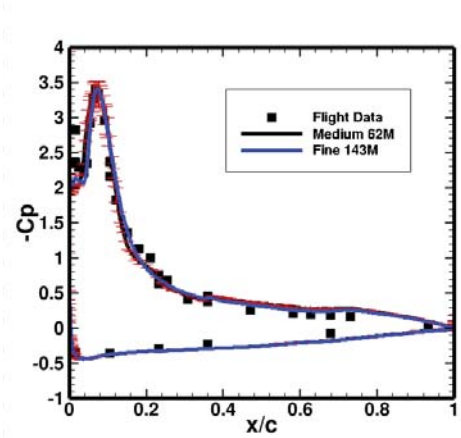

(a) BL 55

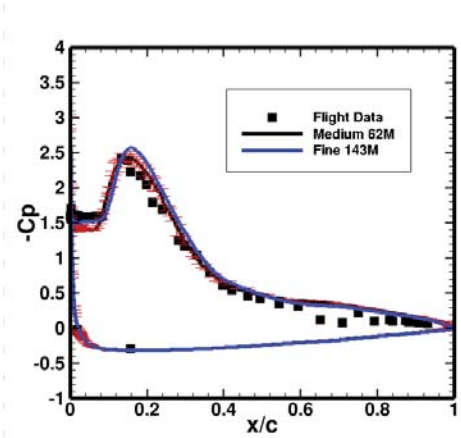

(b) BL 70

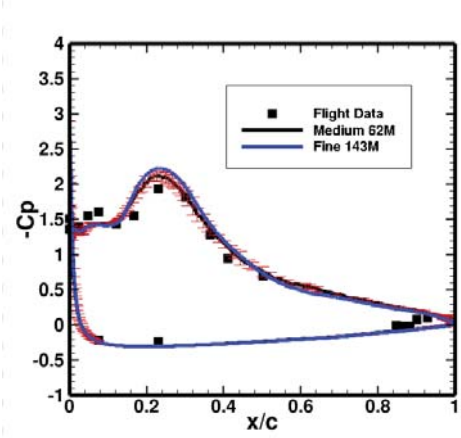

(c) BL 80

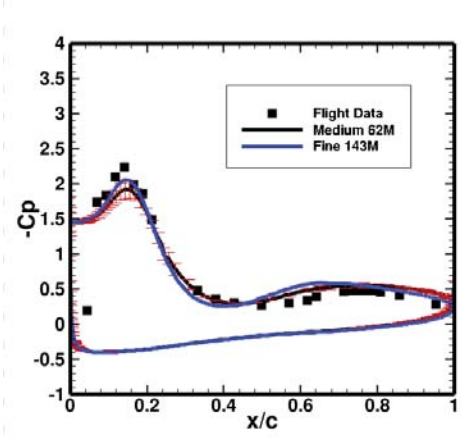

(d) BL 153.5

Figure 8. Computed error estimates on 62M-cell mesh compared with 143M-cell fine mesh results (M_∞ = 0.242, α = 19.84°, Rn= 32.2 X 10^6, kε turbulence model).

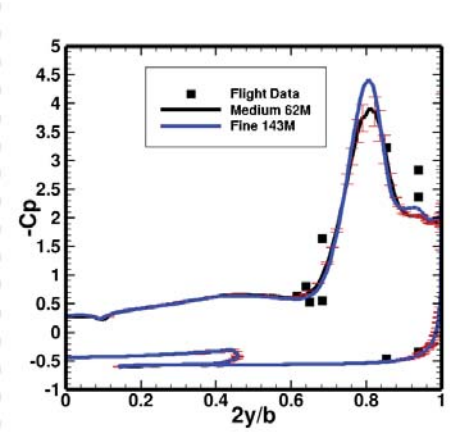

(e) FS 185

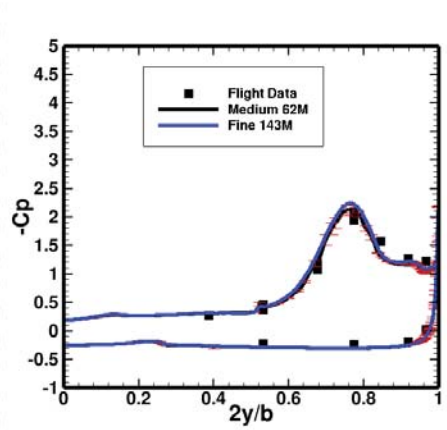

(f) FS 300

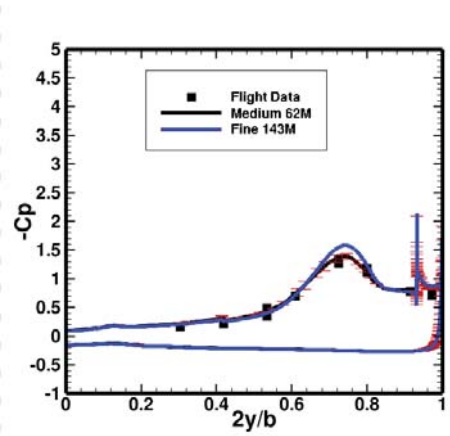

(g) FS 375

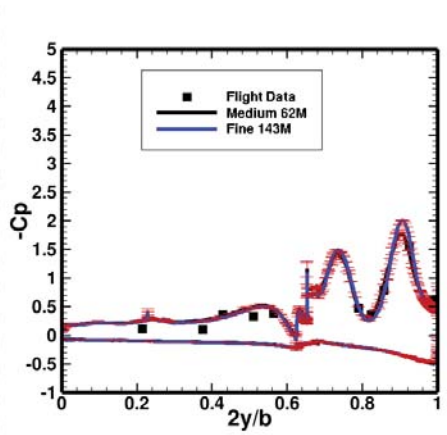

(h) FS 450

Figure 8. concluded.

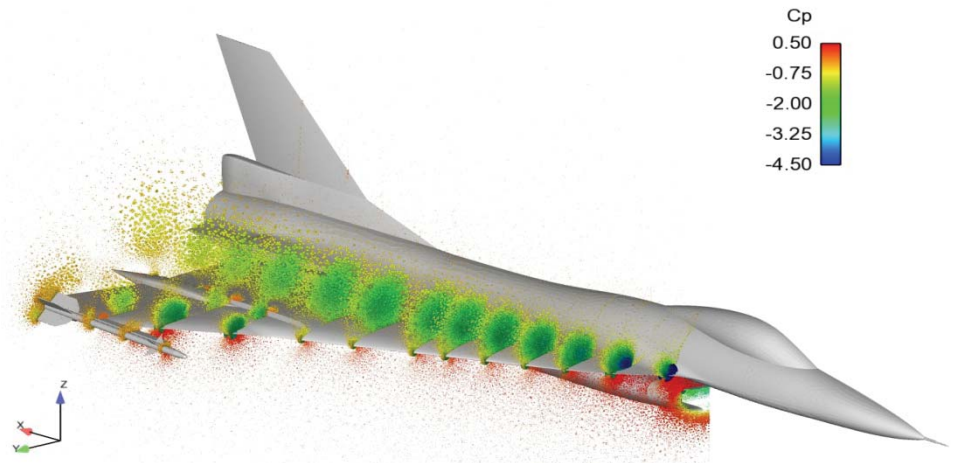

Figure 9. Bubble plot visualization of errors in pressure coefficient for 19M-cell coarse mesh.

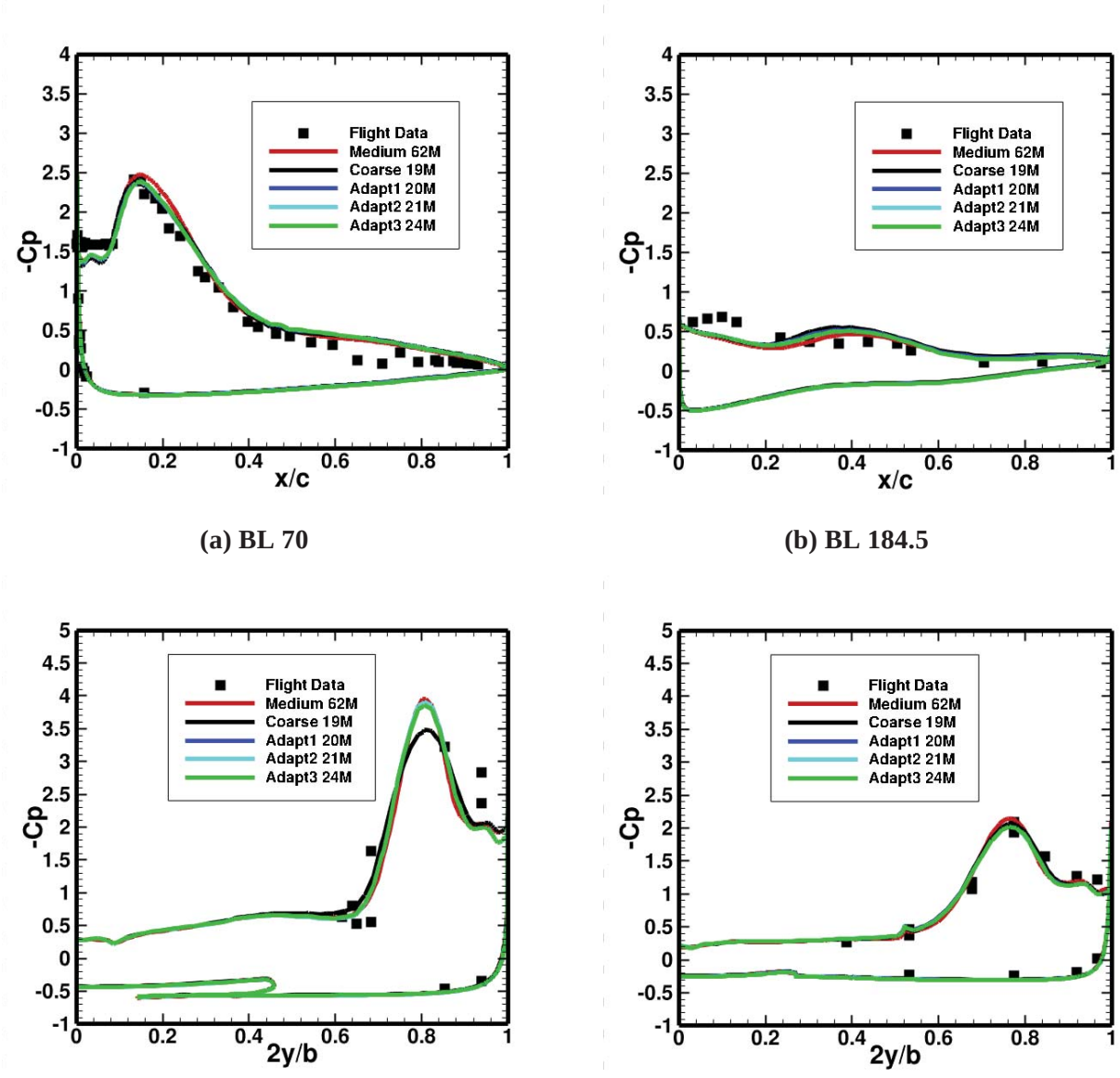

(a) BL 70 **(b) BL 184.5**

(c) FS 185 **(d) FS 300**

Figure 10. Comparisons of computed Cp at different grid adapted levels and measured flight data (M_∞ = 0.242, α = 19.84°, Rn= 32.2 X 10^6, kε turbulence model).